This project has received funding from the Euratom research and training programme 2014-2018 under grant agreement No 662287.

EJP-CONCERT

European Joint Programme for the Integration of Radiation Protection Research

H2020 – 662287

D9.111 - Report summarizing the feasibility of the methods, and the accuracy of personal dosimetry in the real workplace

Lead Authors: Rick Tanner and Olivier Van Hoey
With contributions from: Mahmoud Abdelrahman, Jon Eakins, Luke Hager and Filip Vanhavere

Reviewer(s): Filip Vanhavere
and CONCERT coordination

Work package / Task	**WP9**	**T9.6 (PODIUM)**	**ST9.6.5.1**
Deliverable nature:	**Report**		
Dissemination level: (Confidentiality)	**PU**		
Contractual delivery date:	**M49**		
Actual delivery date:	**M53 (approved postponement)**		
Version:	**1**		
Total number of pages:	**29**		
Keywords:	**Annual report**		
Approved by the coordinator:	**M54**		
Submitted to EC by the coordinator:	**M54**		

Abstract

For PODIUM WP5, which handles the application of the PODIUM approach in mixed neutron-photon workplace fields, two measurement campaigns have taken place. The goal of these measurement campaigns was to evaluate the feasibility of the PODIUM approach in neutron workplace fields and more specifically to investigate how the neutron field can be characterized in an efficient and sufficiently accurate way by measurements and/or simulations.

- The first measurement campaign was in a controlled environment, where all parameters are known, and the neutron field can be well characterised. For this, the PHE calibration facility was chosen, with an adjustment to make the field simulate a real workplace field.
- The second measurement campaign was in a more realistic neutron field, where not all details of the neutron fields were known, and where temperature and environmental conditions can change. Such a realistic neutron field was found at SCK•CEN.

The measurements in this realistic field are the subject of this deliverable. For this SCK•CEN field one MOX transport container was placed at a specific location, so that measurements could be made around this container without disturbing other activities in this hall. This container was filled with MOX fuel rods, so that sufficient neutron dose rates could be measured. Around this container, SCK•CEN and PHE did measurements with as many neutron dosemeters and spectrometers as could be obtained, and an IPS (indoor positioning system from WP1) was also installed at this location. The measurements hence took place from June to September 2019.

TABLE OF CONTENT

1 Introduction

Deliverable D9.111 builds on the work from D9.102 in which the radiation fields were defined and selected, and D9.108 which dealt with the progress in a simulated workplace field. This deliverable describes the progress made towards demonstrating online dosimetry in a real workplace.

A two-stage process is necessary, whereby a dose rate map is generated for a facility for use in the software tool from Work Package 3, rather than real time Monte Carlo. The reasons for not going to full real time simulations for neutrons are given in D9.108. These derive from the relatively slow Monte Carlo calculations for neutrons and the complexity of the workplaces where neutrons are likely to be encountered. Issues with the application of the radiation weighting factor for neutrons currently force such a two-stage process. This means that building up a dose rate map is an important goal in the PODIUM strategy. The strategy for a simulated workplace field can be seen in Figure 1. The strategy for a real workplace field must be amended slightly because there are more unknowns (Figure 2). The strategies applied within PODIUM foresee Monte Carlo simulations. Many workplaces with significant neutron dose rates already have Monte Carlo models which could be utilized by a PODIUM system: models are often used for shielding design and to understand some physics issues. Still, the PODIUM approach could also work only with measurements, although with a larger uncertainty.

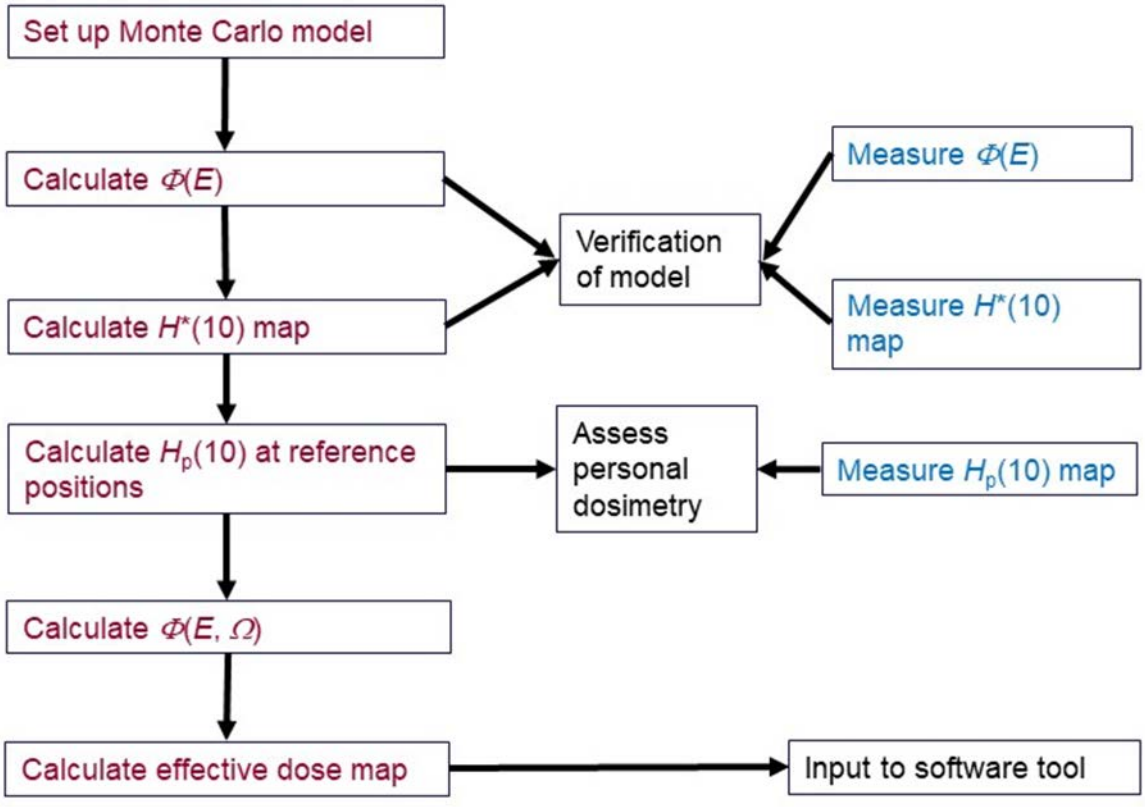

Figure 1. Strategy for workplaces where the source term is well known

In the simulated workplace there is the key advantage that the source is well known. Within PODIUM a ^{241}Am-Be source was used, which is well characterized and described in an International Organization for Standardization standard. If this is true also of a real workplace, then the strategy in Figure 1 could

be adopted there as well. In the real workplace, the source term is not so well defined. The materials in the room may also be less well known, which is important for neutrons, because cross sections vary strongly from element to element but also for isotopes of a specific element. Some materials such as concrete are a persistent problem in this regard. Consequently, the strategy adopted (Figure 2) involves an iterative approach to getting the source term right, with the spectrometry feeding into the model development. It may be necessary to take information from literature surveys to get realistic source spectra, which can then be used in the model. The differences are highlighted using the red lines (Figure 2).

In the present PODIUM strategy, the accuracy of the computer model is tested by verification of the neutron spectrum at key locations. This can be determined by spectrometry using Bonner spheres, or other innovative spectrometers. Additional input to this process comes from measurements using neutron area survey meters, which give assessments of the neutron ambient dose equivalent rate in the workplace. Those measurements can also be corrected using the determined spectrum to improve the agreement.

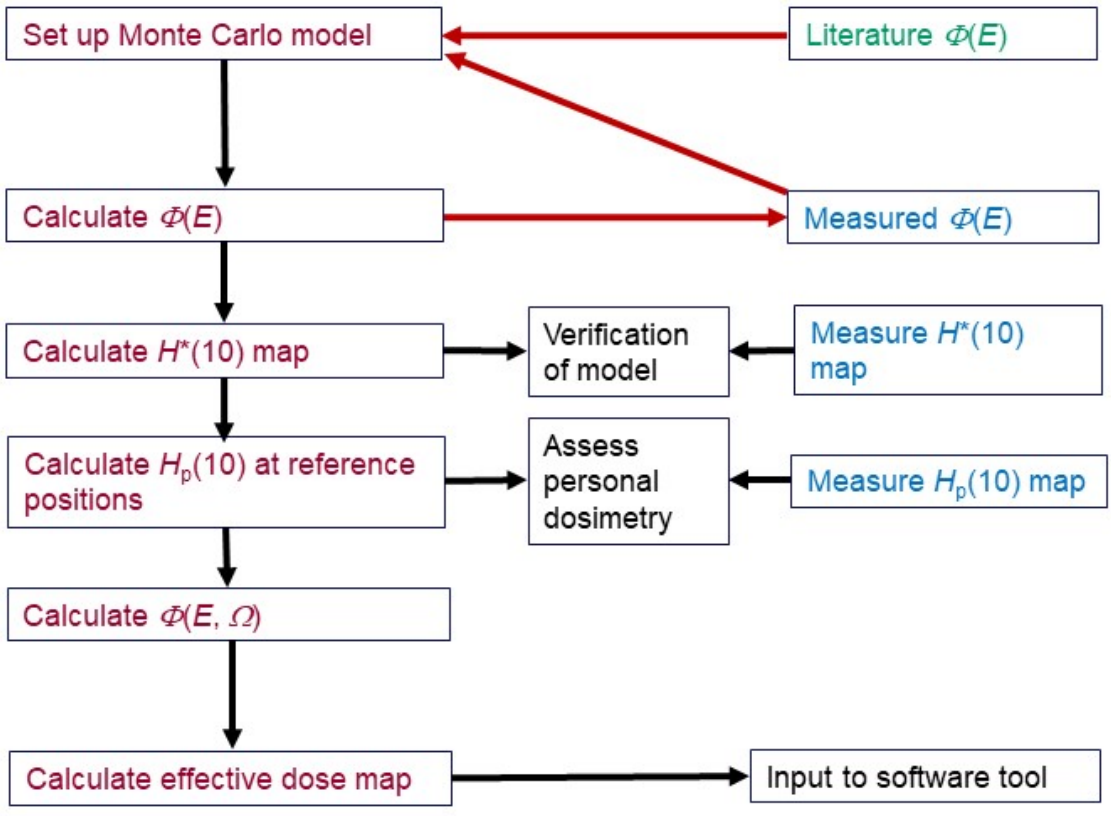

Figure 2. Strategy for workplaces where the source term is uncertain

Besides H*(10) maps and the neutron energy spectrum, also $H_p(10)$ and E maps are ideally needed for the PODIUM approach. This depends not only on the energy distribution of the field, but also on the direction distribution. Given that the total fluence has been verified, it may be assumed that both the relatively unscattered (direct) component of the field and the strongly scattered component are both simulated accurately. Then personal dose equivalent and effective dose can be calculated. Given the

stronger direction dependence of personal dose equivalent, deficiencies in this reasoning will impact more on the estimates of personal dose equivalent than on the estimates of effective dose. The personal dosemeter readings on different faces of a geometric phantom can also be used to verify the direction distribution of the field, especially where they are facing away from the primary direction of the neutron field. In this what they can be part of the characterization process.

Personal dosemeters can be used in this process to assess the state of the art: for comparison with the effective dose estimates. In essence, the question is: can we do better with online dosimetry than we do with personal dosemeters? The relative inaccuracy of neutron personal dosemeters is one of the drivers for this project, so it is not to be anticipated that the results from the Monte Carlo modelling will be in perfect agreement with the personal dosemeter measurements. It needs to be understood that the acceptable range for the response of a personal dosemeter is a factor of two in the estimate of $H_p(10)$ rather than effective dose. In reality the personal dosemeters behave even worse, as can be seen in 2.7. During the tests in PHE and SCK-CEN, as many personal dosemeters as possible have been exposed in the field to make this assessment. Four types of passive personal dosemeter and one active dosemeter were sourced for the measurements. These measurements were long duration, because neutron personal dosemeters are not very sensitive. Typical issue periods for neutron personal dosemeters range from 4 weeks to 6 months or longer, but still reporting thresholds are an issue in most workplaces.

In parallel with the personal dose estimation, effective dose will be estimated using the Monte Carlo results binned for energy and direction, because the effective dose in the field depends on the energy distribution of the field, the direction distribution of the field and the direction that the person is facing. This is the most complex part of the modelling process: it is used to build up the effective dose rate map on an x-y grid in the horizontal plane, with the data for each location being related also to the direction that a person is facing.

2 The SCK•CEN field

The field is representative of infrequent high neutron dose rate activities carried out in the facility. It relates to the storage of high burn-up mixed oxide (MOX) fuel rods inside a thick lead shield (Figure 3). The purpose of the lead is to shield the intense photon field from the fission fragments in the fuel, which is likely to be dominated by Cs-137 photons, although there will be additional photons from the fuel itself as well as other fission fragments. The lead shield is not expected to cut down the neutron dose rate very significantly because neutrons lose very little in elastic scattering events with lead nuclei. Down-scattering in energy should be anticipated, but there should be little thermalization of the field by the lead.

The fuel rods are over 30 years old with a complex history in two different nuclear reactors. They were used in the Belgian Reactor 2 (BR2) until 2014. So specification of the exact source term is not possible, but a “cooling time” of about 5 years can be assumed for this project. Because nuclear facilities will be one of the key targets for the PODIUM system, it is important that this issue can be addressed in this test.

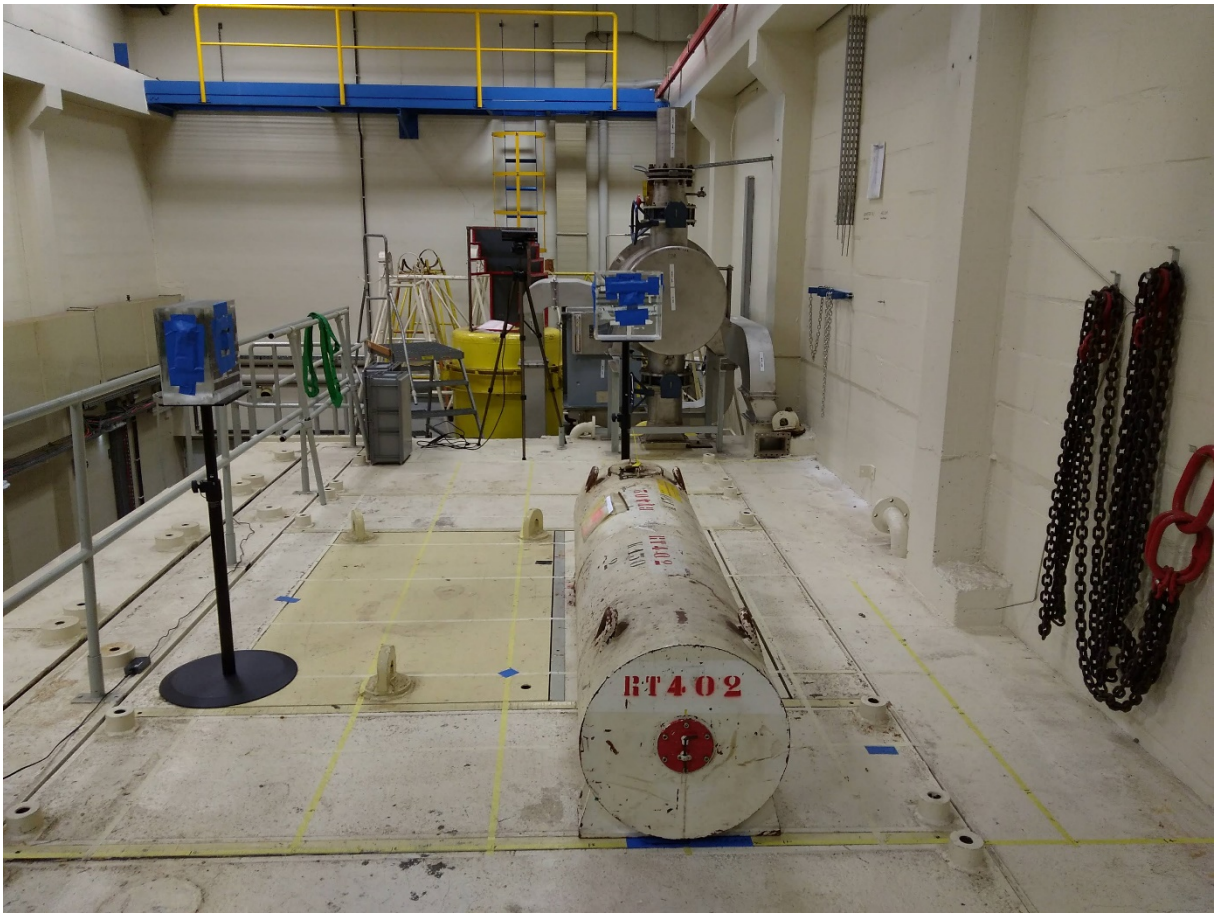

Figure 3. The fuel flask in the measurement position. The grid locations for the field determination are marked by tape on the floor. This figure shows two ISO slab phantoms with personal dosemeters mounted for determination of the accuracy of personal dosemeters.

2.1 The workplace

The fuel flask was in a quiet part of the facility (Figure 3), resting on a concrete floor. There was a lead shield in the floor, to reduce dose rates from a cell below, and a drop to a lower floor on two sides. The concrete wall is closer on one side and there are metal objects (chains) on the wall that may provide significant scatter. The ceiling is relatively high and the walls on two sides of the room relatively distant. Complex equipment is located beyond each end of the room beyond the ends of the flask, but distance makes it unlikely that this needs to be included in the MCNP model.

The key aspects of the room to simulate are the concrete walls and floor and the lead shield within the floor. It was decided that other small features would be omitted, unless there was strong evidence from the measurements that they should be added to the model.

The flask (Figure 4) contained four fuel rods, which were located inside the internal cavity. The precise location of these fuel rods could not be known, without opening the fuel flask to inspect them, which would incur significant photon and neutron doses. For the purposes of this deliverable, it is assumed that they are located in the centre of the fuel flask, resting on the bottom of the inner cavity.

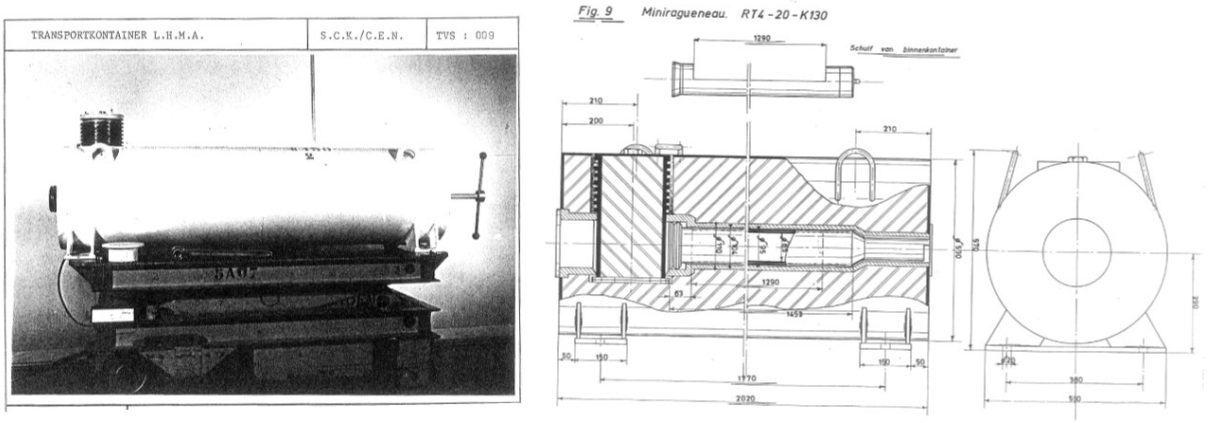

Figure 4. The fuel flask. Left, a photograph of an equivalent fuel flask; right, technical drawings of the design

The workplace was labelled using an x-y grid (Figure 5) with 25 cm spacing, and at 3 different heights (18-55-125 cm). This was used for fine grid measurements using neutron survey instruments and for modelling the field. Subsequent tracking of people will be done using this grid. Reference positions were added to this grid for additional characterization of the field using personal dosemeters and Bonner spheres. These are labelled positions A-G. Most were at 1.25 m height to represent a standing person. Positions C and F are at the same (x,y,z) location, but F is rotated by 45° around the z-axis relative to position C to test personal dosemeter sensitivity to direction: for $H^*(10)$ they are equivalent. A, the highest dose rate location, was chosen to be 55 cm to represent a crouching person working on the flask, and E was chosen to be 18 cm high.

The focus for the measurements and characterization was on the left side of the field as viewed in Figure 3. This was because a person passing by the flask would naturally pass on that side owing to the greater space. Reference points were chosen to relate to standing person except for one lower position, which was considered to be the worst-case scenario of a worker crouching to take a contamination measurement of swab from the flask. Inverse square considerations, and the location half way along the flask would make this the highest dose rate that a worker could feasibly experience.

2.2 The fuel rods

The fuel rods were 30 years old and there was no detailed information available on the precise fuel composition or burn-up. It was anticipated that these would be key factors in determining the neutron spectrum and the emission rate, but the sensitivity of the results to the specification of the source is an important test for this real workplace application.

The emission rate is not determinable from the information available, but that is not a significant problem: there will be plentiful experimental data that can be used to normalize the total fluence.

	x_{label}	0	1	2	3	4	5	6	7	8	9	10	11	12	13	14	15	16	17
	x (m)	0	0.25	0.5	0.75	1	1.25	1.5	1.75	2	2.25	2.5	2.75	3	3.25	3.5	3.75	4	4.25
y_{label}	y (m)																		
7	1.75																		
6	1.5					C, E, F			D										
5	1.25																		
4	1																		
3	0.75																		
2	0.5					A													
1	0.25	Fuel Flask																	
0	0										B								
-1	-0.25																		
-2	-0.5																		
-3	-0.75																		
-4	-1					G													
-5	-1.25																		
A	position (4,2)		B	position (9,0)		C,F	position (4,6)		D	position (7,6)		E	position (4,6)		G	position (4,-4)			
	height 55 cm			height 1.25 m			height 1.25 m			height 1.25 m			height 18 cm			height 1.25 m			
						F rotated 45°													

Figure 5. The x-y grid for designating the field. The positions A-G were selected for additional measurements.

2.2.1 MOX fuel

Mixed-oxide fuel is generally a mix of UO_2 and PuO_2, with the uranium being unenriched. Typically, the plutonium to uranium ratio is about 7:93, though this will change during use because of both the fission that takes place and the neutron capture that introduces higher A isotopes and consequently higher Z elements via beta decay.

MOX fuel in a sub-critical state emits neutrons via spontaneous fission and (α,n) reactions. The ratios of these, and the elements responsible, change with the degree of burn-up and the cooling time [Shimanskaya, 1980b, Shimanskaya, 1980a, Sasahara et al., 2004]. Few isotopes have significant (α,n) cross sections because the Coulomb repulsion is too great. This is especially true for high Z elements, but also for isotopes such as ^{16}O. Notable exceptions are ^{6}Li, ^{7}Li, ^{9}Be, ^{10}B, ^{11}B, ^{17}O and ^{18}O. In the case of MOX fuel, the two oxygen isotopes are crucial, though ^{17}O constitutes only 0.038% of natural oxygen and ^{18}O 0.204%. The cross section for ^{18}O peaks at about 0.8 b whereas that for ^{17}O peaks at about 0.4 b [Soppera et al., 2017], so clearly owing to its 5 fold greater incidence and higher cross section, ^{18}O should dominate the (α,n) production of the fuel. However, a confounding factor is the negative Q-value for ^{18}O, which will lead to lower energy neutrons than are emitted by ^{17}O, which has a positive Q-value (Table 1). However, both reactions have very small Q-values when compared to that for ^{9}Be, the best characterized emission spectrum.

Neither MCNP6 [Pelowitz, 2013] and MCNPX [Pelowitz, 2005] include (α,n) cross section data, so even though they can transport α-particles, they cannot be used to generate (α,n) spectra. The most obvious spectrum to use for the (α,n) component of the field is ^{241}Am-Be [ISO, 2001], but the neutrons from oxygen will inevitably have lower energy because of the lower Q-value. The spectrum is reported to have a peak in the region 2.5-3 MeV and a maximum energy of about 5 MeV [Shimanskaya, 1980a], which compares with the mean of 4.4 MeV for ^{241}Am-Be, for which the maximum neutron energy is over 15 MeV.

Table 1: data for key isotopes for (a,n) reactions

Isotope	Maximum cross section	Threshold α-particle energy	Q-value
^{9}Be	0.8 b	~ 2 MeV	5.70 MeV
^{17}O	0.4 b	~ 2 MeV	587 keV
^{18}O	0.8 b	~ 3 MeV	-696 keV

The key factor that changes the ratio of (α,n) to spontaneous fission neutrons is the in-growth of the curium isotopes, ^{242}Cm and ^{244}Cm [Ensslin, 1991]. These have high spontaneous fission decay rates but are only created in the fuel after multiple neutron captures and β-decays. Of the two, ^{244}Cm has the longer half-life and hence it dominates once the fuel has spent about a year cooling [Shimanskaya, 1980b]. The (α,n) reactions are also stronger in fuel that has not spent a long time cooling because of short lived α-emitters that have been generated in the reactor, so there is a more rapid decline in those reactions than there is in the spontaneous fission: after about 2 years cooling the (α,n) component of the field should be less than 5% of the total neutron emission [Shimanskaya, 1980a].

Table 2. Relative fractions of spontaneous fission and (α,n) neutrons from MOX fuel versus cooling time [Shimanskaya, 1980a]. The fuel in this work had a cooling time of about 5 years, but these fractions will also be dependent on the burn up of the fuel.

Cooling time (y)	Spontaneous fission component	(α,n) component
0	83.0%	17.0%
1	90.3%	9.7%
2	94.9%	5.1%
3	96.2%	3.8%
5	**96.0%**	**4.0%**
10	95.6%	4.4%

Because the fuel is known to be high burn-up, and to have been removed from storage for these experiments, it is initially assumed to have a dominant spontaneous fission neutron yield, though tests using a ^{241}Am-Be energy distribution have also been used to check for sensitivity. This seems reasonable in the absence of a credible ^{18}O(α,n)^{21}Ne spectrum. The results will still need to be normalized to fit experimental data using the reference neutron survey instrument for this project [Eakins et al., 2017] and the results from Bonner spheres.

2.2.2 Generation of the spontaneous fission spectrum

To test for isotopic sensitivity of the spontaneous fission spectrum on the isotopic mix, there are two options available in MCNP6.1: use the simple Maxwell distribution or the detailed emission spectrum for specific isotopes. The latter was preferred on the grounds of greater accuracy. The model for this stage used only a representation of the fuel rod (Figure 6).

The results from doing this (Figure 7) show relatively weak sensitivity to element or isotope, though the spectrum for ^{239}Pu differs significantly from the others, being lower in mean energy, though ultimately the impact on the dose rate in the workplace is the sensitivity that is important. However, given that the yield from ^{239}Pu is expected to be orders of magnitude lower than those from curium isotopes [Ensslin, 1991], so given the similarity between the other energy distributions it is considered that either an average spectrum or the ^{242}Cm spectrum can be used as the emission spectrum.

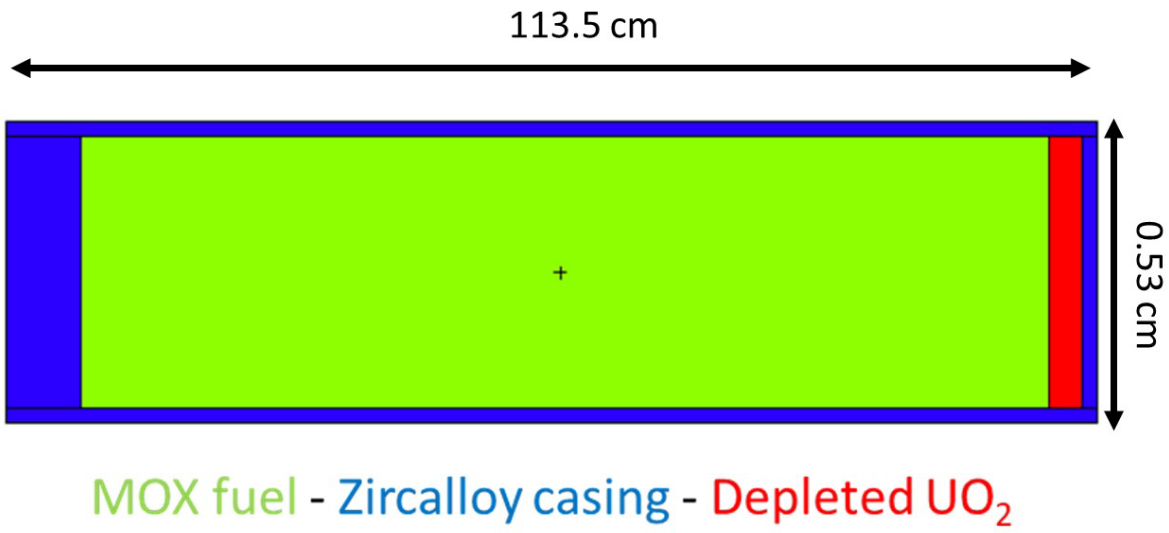

Figure 6. MCNP setup of the simplified fuel rod (note the horizontal and vertical scales are different)

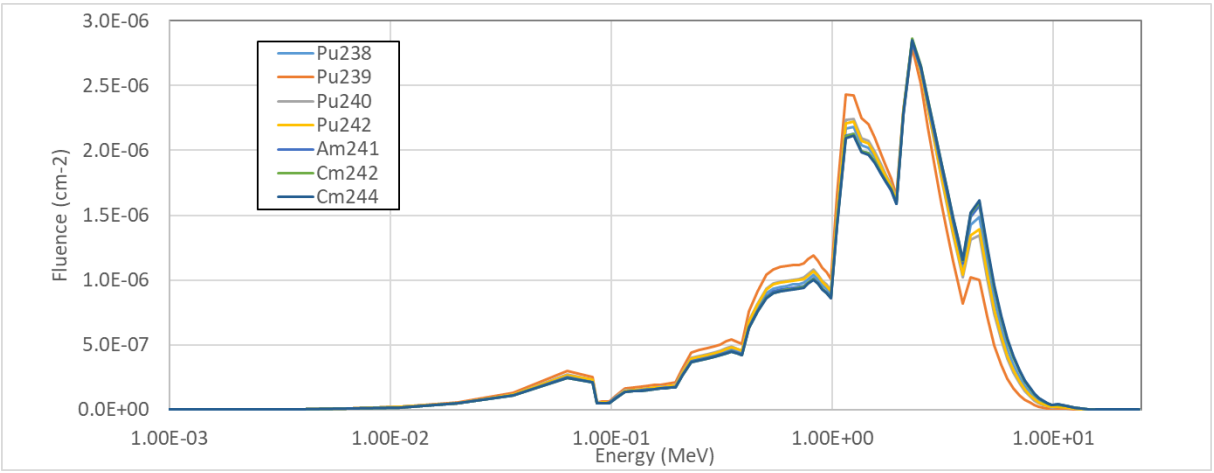

Figure 7. Spontaneous fission spectra from the model of the fuel rod (Figure 5).

2.3 Modelling the fuel flask

The fuel flask has been modelled using both the average ^{241}Am-Be (Figure 8) and spontaneous fission (Figure 9) spectra. These show spectra with very similar energy distributions, which is reassuring in terms of uncertainty and the possibility of applying MCNP in nuclear fuel cycle locations where the source is not well known. The difference in the magnitude of the fluence for the two different sources is of no concern because normalization to the Bonner spheres or survey instruments is still required.

Position A has the highest fluence rate, which is anticipated because of inverse square effects. No data are shown for Position F because that is a simple rotation of Position C, which alters the $H_p(10)$ but not the fluence or $H^*(10)$.

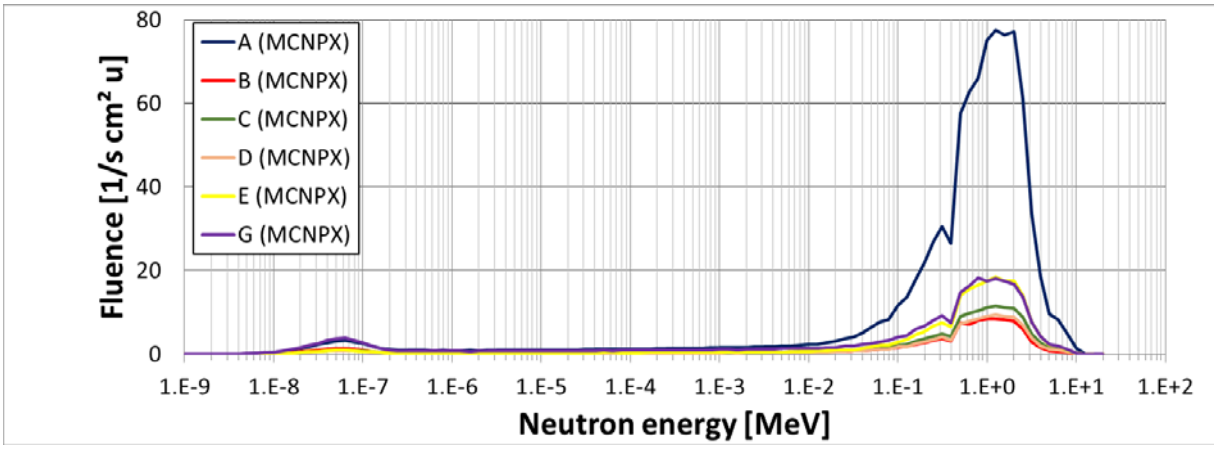

Figure 8. Spectra for the reference positions for the field modelled using a ^{241}Am-Be energy distribution for the source

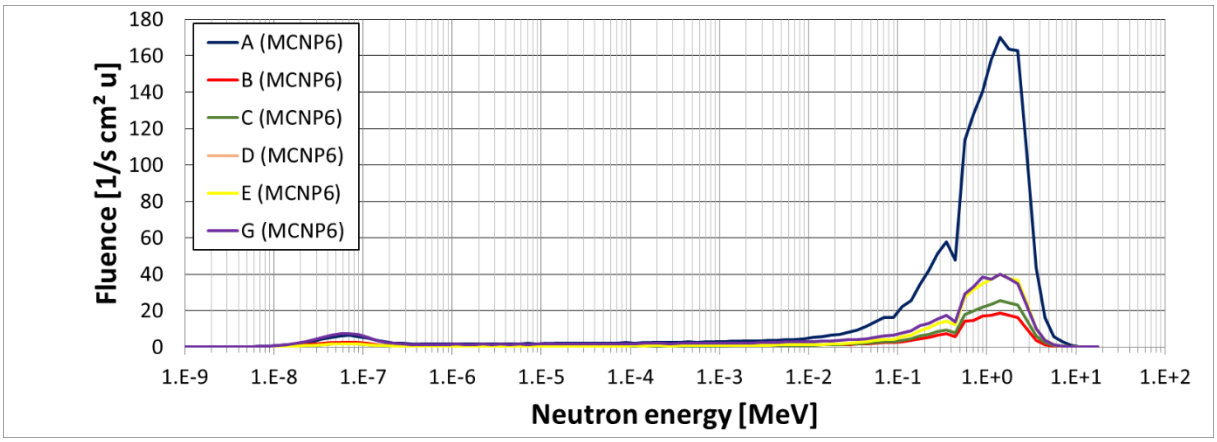

Figure 9. Spectra for the reference positions for the field modelled using a spontaneous fission energy distribution for the source. The difference in the y-axis scale is not important because these data need normalization to survey instrument or spectrometer results.

The comparison between the two sources for Position A after normalization shows that the fields are not very different. They have thermal neutron components that are negligible but almost identical in magnitude, very little in the way of intermediate neutrons and fast peaks with a maximum between 1 and 2 MeV. The fast peak for the ^{241}Am-Be source is a bit broader in energy, but this has very little impact on the fluence weighted average $H^*(10)$ conversion coefficients for the two computations (Table 3): the spontaneous fission source produces 3-4% higher values, which is insignificant compared to other experimental uncertainties.

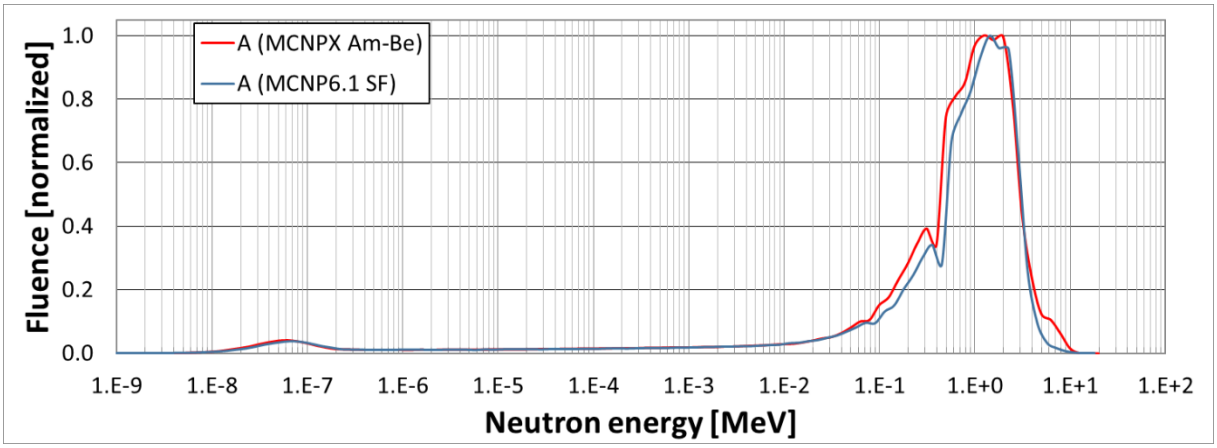

Figure 10. Comparison between the results for Position A, normalized, for spontaneous fission and ^{241}Am-Be sources

Table 3. Monte Carlo calculated fluence averaged conversion coefficient, $H^*(10)/\Phi$ (pSv cm^2), for a ^{241}Am-Be source (α,n) and a spontaneous fission source [Oatway and Mobbs], versus location

Location	MCNPX, (α,n) (pSv cm^2)	MCNP6.1, SF (pSv cm^2)	Ratio: SF/(α,n)
A	312	322	1.03
B	257	266	1.04
C	287	296	1.03
D	283	292	1.03
E	303	313	1.03
G	242	249	1.03

2.4 Experimental spectrometry

Two different methods of performing the spectrometry experimentally were used: Bonner spheres and a DIAMON detector[1] (Figure 11). The Bonner spheres require a sequential set of measurements in a location (taking about 2 hours in total per location) whereas the DIAMON can make the field determination in a single measurement (taking about 10 minutes per location). Furthermore, the DIAMON also has real-time deconvolution using a parametric description of the neutron fluence energy spectrum.

2.4.1 Bonner spheres

For the Bonner sphere measurements, a set of 8 spheres (3", 4", 5", 6", 7", 8", 10" and 12") and a Centronic SP9 spherical ^{3}He proportional counter were used. The response functions were simulated using MCNP and validated by measurements with the bare proportional counter in the thermal neutron beam of the SCK•CEN Belgian Reactor 1 (BR1) and with the 8" sphere at the SCK•CEN Laboratory for Nuclear Calibration with Cf-252.

Two different unfolding methods were used with the Bonner sphere data: the programs FRUIT [Bedogni et al., 2007] and an algorithm developed by SCK•CEN and PTB in Winbugs [Lunn et al., 2000] were applied. Both methods use the same parametric description of the neutron fluence energy spectrum. However, FRUIT uses a simple random walk like approach to find the optimal parameters, while the algorithm in Winbugs uses a Bayesian approach. As the unfolding is a strongly

[1] https://www.raylab.solutions/wp-content/uploads/2018/10/DIAMON_brochure.pdf

underdetermined mathematical problem one can expect differences between the two methods. There are indeed some evident differences between the Winbugs (Figure 12) and FRUIT (Figure 13) results.

The thermal peaks are very similar for both programs but there is a much stronger intermediate component for Position B in the FRUIT results; Position D produces a much narrower fast peak using FRUIT; Position G has a lower peak energy using FRUIT.

At a later stage also two other unfolding codes MAXED [Reginatto et al., 2002] and GRAVEL [Matzke, 1997] will be used. These unfolding codes start from a guess spectrum. These unfolding methods will be tried using the spectra from the MCNP simulations as guess spectra.

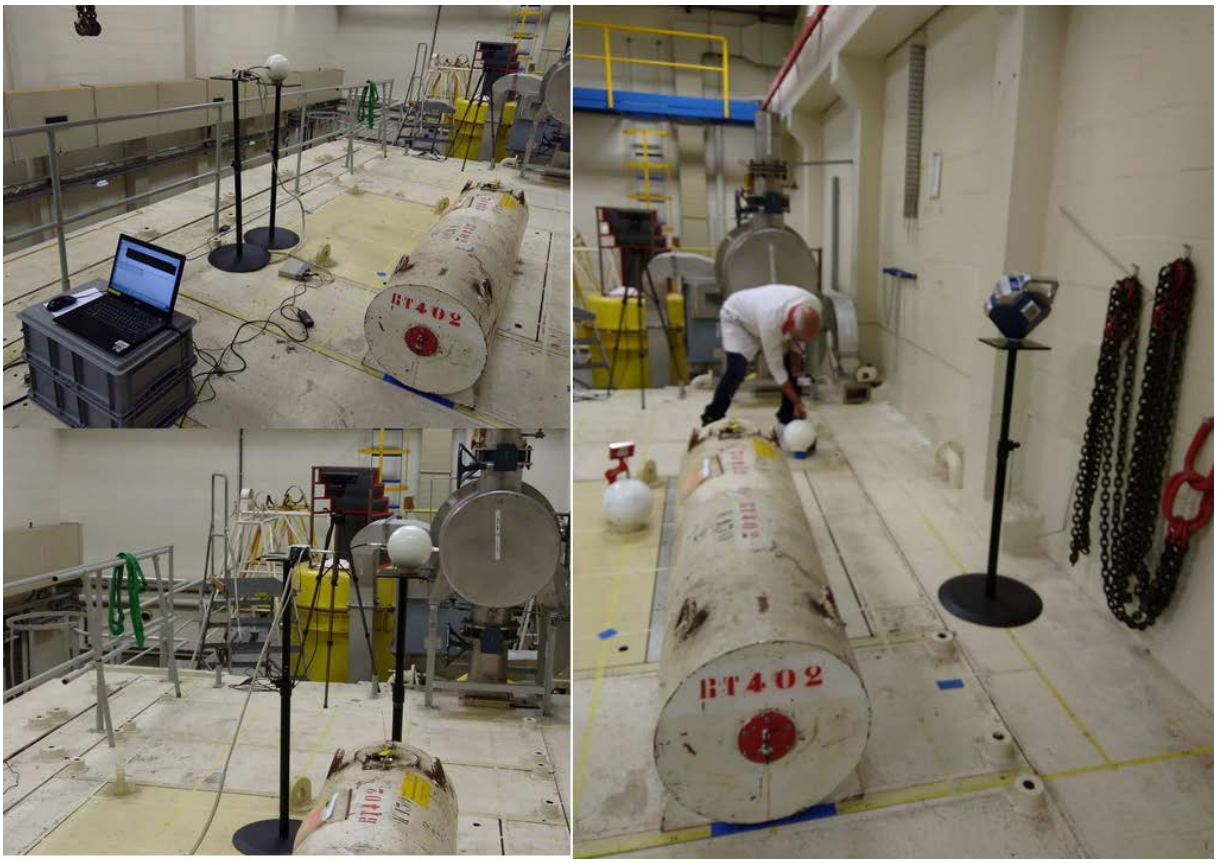

Figure 11. Spectrometry measurements: left top and bottom Bonner spheres; right the DIAMON instrument

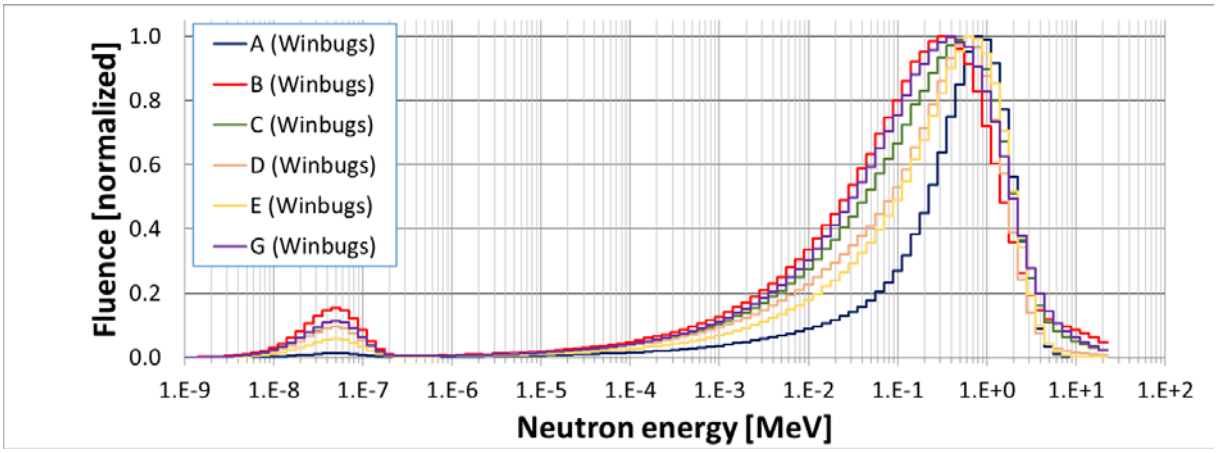

Figure 12. Spectra for the six distinct locations (F ≡ C) unfolded from the Bonner sphere readings using Winbugs

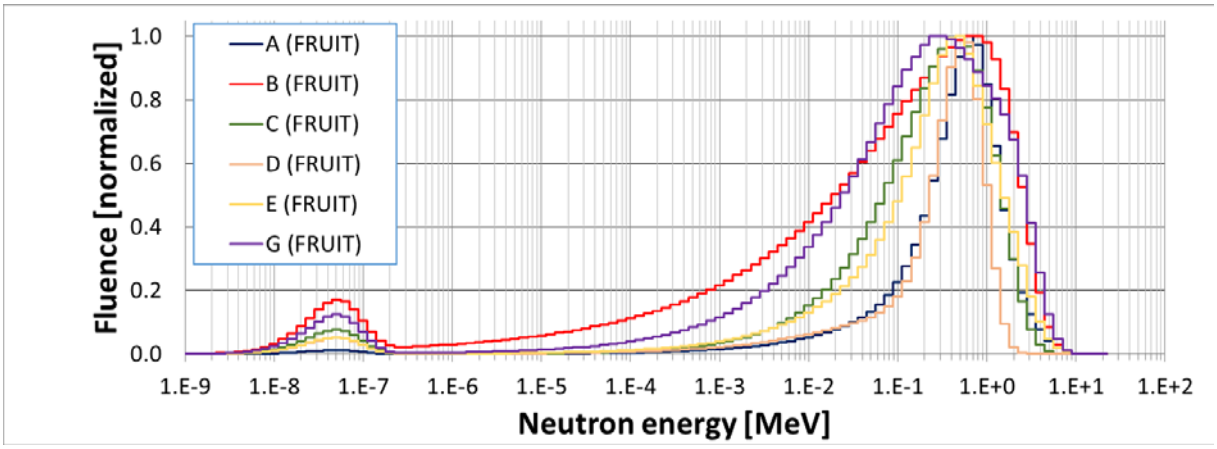

Figure 13. Spectra for the six distinct locations (F ≡ C) unfolded from the Bonner sphere readings using FRUIT

2.4.2 DIAMON

The DIAMON instrument uses a concentric array of detectors within a single polyhedral moderator. It unfolds the spectrum in real time and can hence give a very quick result for the field (Figure 14). The main features of these spectra are visually similar to those from the Bonner spheres, though the fast peak is strictly fixed in energy. This probably derives from the parameter based unfolding method which may not be able to vary as many features of the field as is possible in Bonner sphere unfolding.

Currently, the DIAMON calculates the total neutron spectrum and the $H^*(10)$ rate, though in real time it can give information on the direction of the neutron field. This capability was evident during measurements when it could detect the contributions from scattering objects. Development of this aspect of the response could lead to direct estimation of effective dose, which would enable dose rate mapping of a workplace without the need for either Bonner spheres or Monte Carlo calculations. Further development and validation is, however, required.

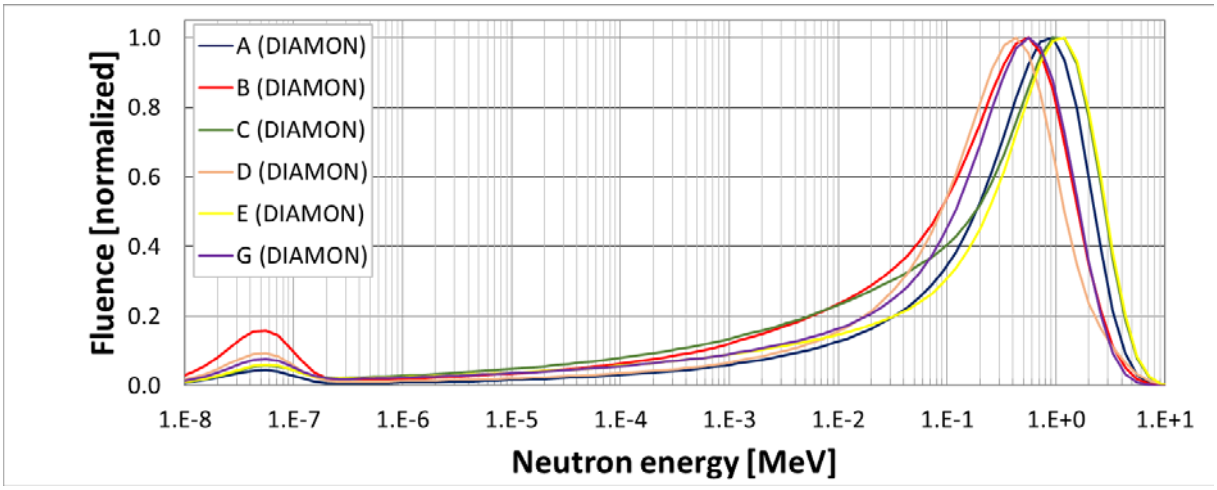

Figure 14. Results for the normalized energy distribution from the DIAMON detector

2.5 Spectrometry summary

The measured and calculated spectra are compared in Figure 15. The Bonner sphere and DIAMON spectra have lower energy fast peaks than the Monte Carlo solutions. This will be investigated in the future with the Monte Carlo results being used as pre-information for the Bonner sphere unfolding.

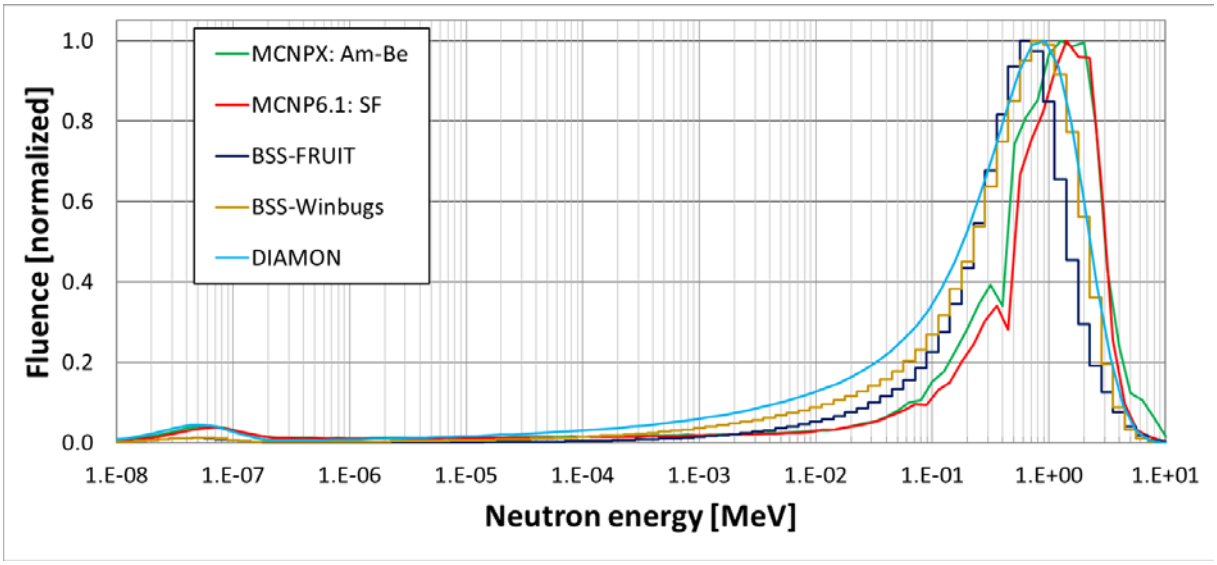

Figure 15. Summary of the spectrometry results, both experimental and from Monte Carlo for Position A

As may be anticipated from the comparison of the spectra (Figure 15), the lower energy of the fast neutron peak from the experimental spectrometry gives lower fluence weighted conversion coefficients for the fields in the reference locations. The differences range from +21% for the most significant location, A, to +53% for B. The results for B are almost certainly caused by the model having insufficient shielding at the end, where the technical drawings of the flask are least clear and the geometry most complex. This will be addressed by refining the model.

Table 4. Experimentally determined fluence averaged conversion coefficients, $H^*(10)/\Phi$ (pSv cm^2) for the six locations determined using the Bonner spheres with FRUIT or WinBugs, and the DIAMON. The results are compared to the mean Monte Carlo (MC) result.

Location	FRUIT (pSv cm^2)	WinBugs (pSv cm^2)	DIAMON (pSv cm^2)	Mean MC (pSv cm^2)
A	277	269	243	317
B	164	169	178	261
C	206	195	209	292
D	236	196	191	288
E	223	220	236	308
G	184	186	199	245

2.6 Survey instrument measurements

A total of five different types of neutron survey instrument were used for these measurements as part of the field verification process (Figure 16):

- GNU, a spherical moderator-based design that is very well characterized in terms of response versus energy and direction [Eakins et al., 2017]
- LB6411 a spherical moderator type [Klett and Burgkhardt, 1996, Burgkhardt et al., 1997]
- Tracerco T405- smaller spherical moderator [Leake et al., 2004]
- WENDI – a moderator type with a cylindrical moderator [Olsher et al., 2000]
- PRESCILA – scintillator design [Olsher et al., 2004]

It is important to recognize that neutrons survey instruments are known to give results with systematic biases, but those biases are predictable when the energy distribution is known [Tanner et al., 2007]. The instruments are all calibrated in terms of $H^*(10)$ and have been used to determine the dose rate at the six reference positions ($H^*(10)$ for C≡F): the results confirm that the dose rate at A is significantly higher than that at any of the other positions (Figure 17).

Figure 16. Survey instrument measurements, left to right: GNU at 18 cm; PRESCILA at 125 cm; GNU at 125 cm; Tracerco T405 at 18 cm.

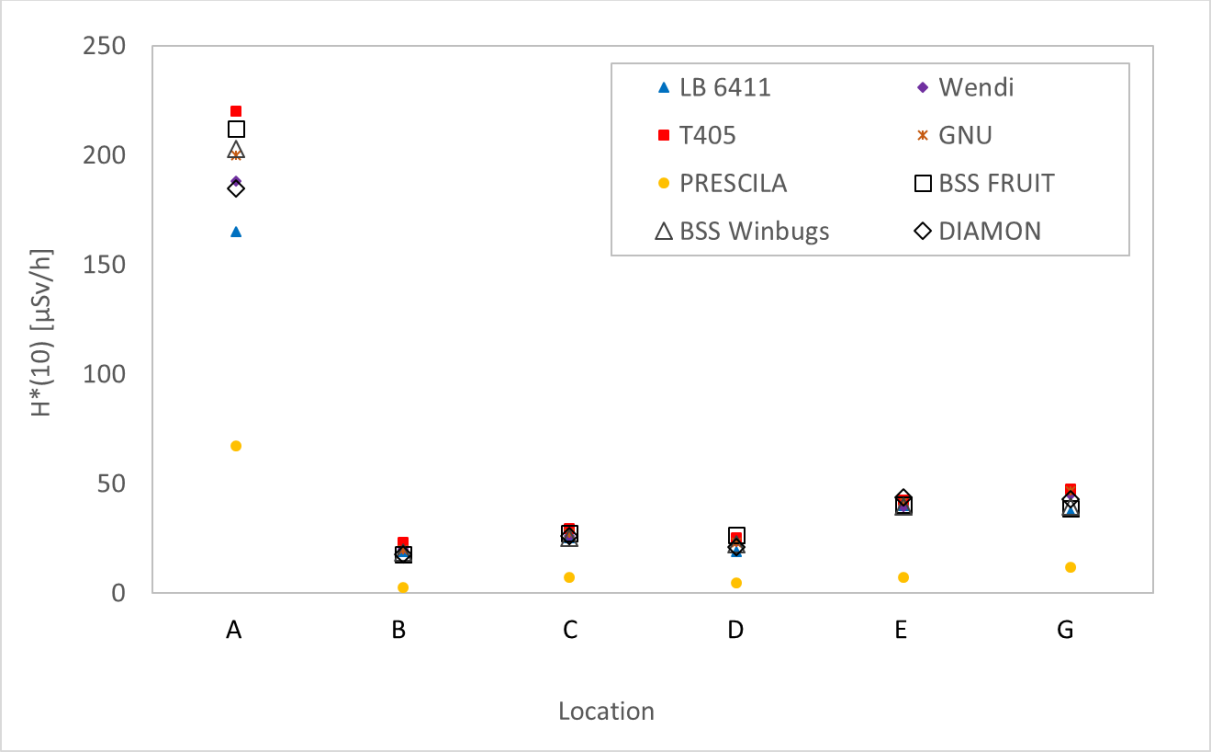

Figure 17. Comparison between the results from the Bonner sphere estimates of H*(10) rate and the survey instrument estimates.

At this stage any normalization of the dose rate data is somewhat arbitrary. An initial comparison uses the average Bonner sphere result for the normalization (Figure 18) on the basis that these may be expected to provide the most reliable result, given that they are intrinsically corrected for the spectrum. The striking feature of these data is the low response of the PRESCILA in all locations. Inspection of the response of this instrument [Olsher and Seagraves, 2003] is the very significant under-response that is has in the energy range 500-800 keV. This is hence a strong indicator that the fast neutron peak of the field is in that energy range.

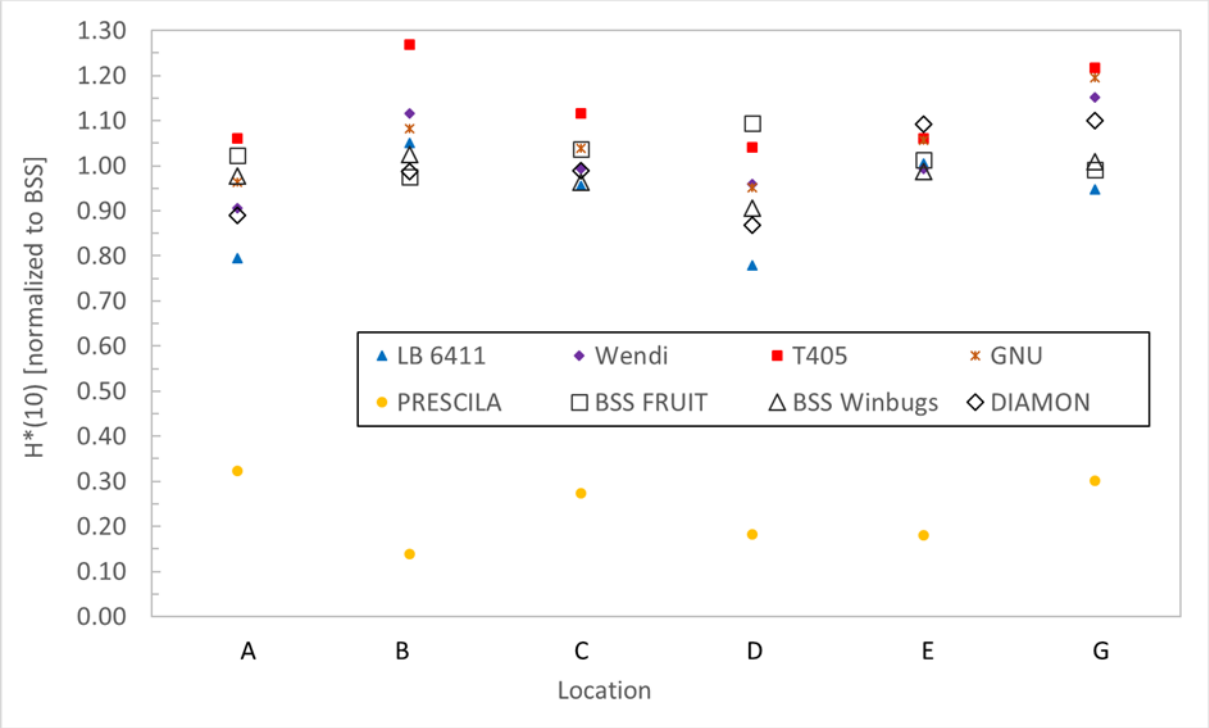

Figure 18. Comparison between the results from the Bonner sphere estimates of normalized H*(10) rate and the survey instrument estimates.

The DIAMON detector and the Bonner spheres differ from the survey instruments because they determine the spectrum and then use that to determine the *H**(10). Conversely, the survey instruments attempt to evaluate the *H**(10) in a manner that does not depend strongly on the spectrum. In this case, there is generally very good agreement between the DIAMON and the Bonner spheres: the poorest agreement is for position D, but there the DIAMON agrees closely with the Winbugs result, which differs by over 20% from the FRUIT result. The Bonner sphere results differ because FRUIT (Figure 13) generates a much narrower fast neutron peak than Winbugs (Figure 12).

More puzzling is the under-response of the LB6411 in positions A and D. That instrument under-responds to thermal neutrons and around 100 keV [Burgkhardt et al., 1997], but none of the solution spectra have strong components of dose in either energy range. Similarly, the over-response of the T405 for position B should require significant epi-thermal contribution, but none of the spectrum determinations indicate that. The DIAMON response is highest for G, where the WENDI, GNU and T405 also over-respond. This is the position closest to the wall, so there may be more scatter from the wall than is being accounted for.

Generally, the survey instruments offer strong support for the Bonner sphere results. The agreement is mostly within 10%, which is a good result in neutron dosimetry.

2.7 Personal Dosimetry

Four passive personal dosemeter types were used in these measurements as well as one active design:

- Landauer Neutrak®[2] chemical etched track dosemeter (CETD)
- PHE electrochemically etch track dosemeter [Hager et al., 2017] (ECETD)
- Thermoluminescent albedo dosemeter (TLAD)
- Chemically etched track dosemeter with thermal TL element (CETDTL)
- Thermo-Fisher EPD-N2 active personal dosemeter (APD)

The aims of the measurements were three-fold:

- Determine the accuracy of personal dosemeters in the workplace
- Provide supporting evidence for the direction distribution of the field
- Allow the merits of the PODIUM approach to be compared to the state of the art using physical personal dosemeters

Figure 19. Personal dosemeter exposures in reference positions

All five dosemeter types were placed as close as possible to the centres of the front faces of ISO slab phantoms, located at various positions (A, B, C, D, E and F) and orientations within the field; in all cases, the front face was identified as that closest to the source. In a first experiment, two slab phantoms (positions A and C) had their front faces 'covered' by 16 PHE dosemeters, to check for dose gradient effects. Dosemeters were also placed on other sides of the phantoms to estimate direction components of the neutron distribution.

The positioning and results from the 16 PHE dosemeters exposed at positions A and C are shown in Figure 20, given relative to the reference $H^*(10)$ value at those positions; although not interpretable as a direct comparison, use of this normalization permits a useful comparison. In both cases, it is seen that the dose rate increases from top to bottom and from left to right, as expected from the survey instrument measurements. Overall, there is up to a factor of 2 difference between different positions on the same phantom for position A due to spatial dose rate gradients. This has to be kept in mind when comparing the personal dosemeter results. However, it is noted the typical uncertainty expected

[2] https://www.landauer.com/sites/default/files/product-specification-file/Neutrak_0.pdf

for the PHE PADC dosemeter is ~20% for a repeated measurement [Gilvin, 2018]. Nevertheless, Figure 20 demonstrates a weakness in single point-of-test dosimetry, and in turn a potential advantage of the PODIUM approach.

Position A: Hp(10)/H*(10)

0.65	0.73	0.80	0.91
0.77	0.89	0.91	0.89
0.99	1.09	1.15	1.27
1.25	1.21	1.47	1.44

Average: 1.03
Stdev: 24%
Max/min: 2.2

Position C: Hp(10)/H*(10)

0.86	0.86	1.06	0.94
0.87	0.95	0.77	1.06
0.98	1.12	0.93	-
1.02	1.24	1.03	1.17

Average: 0.99
Stdev: 13%
Max/min: 1.4

Figure 20. Position and results from the 16 ECETDs 'covering' the phantom front face.

Figure 21 shows the results of the five dosemeter types at positions A, B, C and D, and Figure 22 provides data at E, F and G, with all results again normalized to the respective $H^*(10)$ value. It is seen that:

- TLAD provides a low result in most cases; although this is not strictly an under-response, due to the normalization to ambient dose equivalent rather than personal dose equivalent: however, for pure frontal exposures the two quantities might be expected to be broadly similar.
- APD also provides a lower value at locations A, B and E when placed on the front of the phantom, but higher values when placed on the right side of the phantom at locations B and G and also at location G when placed on the left or back.
- CETDTL also provides a high value when placed on the right side of the phantom at location B, for which one ECETD recorded a zero value, likely due to a processing error.
- All dosemeter results were low at location F, for which the phantom was orientated at 45° to the flask, but of course the $H_p(10)$ response of a dosemeter is expected to be lower than $H^*(10)$ for acute angles >0°.
- Low results were also found at location G, likely due to the same reason and attributable to neutron scatter from the wall adjacent to that position.

Overall, the direct (i.e. 'frontal') dose component was found to be dominant in all cases, as anticipated. Moreover, the reduction in $H_p(10)$ with angle relative to $H^*(10)$ is also expected. The important next test will therefore be to evaluate whether these findings are consistent with the results from Monte Carlo simulations, which will proceed once the model is complete and has been fully verified. The

trends and comparisons in Figure 21 and Figure 22 are as expected: ECETD and CETD give $H_p(10)$ results that are typically within 40 % of the $H^*(10)$ value, and generally consistently lower; the results from CETDTL and APD are more variable with location; and TLAD appear consistently low. The results of these 5 routinely used well established personal neutron dosemeters differ with a factor of 4 in our realistic field. This type of variability once again indicates the potential power of the PODIUM approach, given the current limitations of both the operational dose quantity and the dosemeters used to evaluate them.

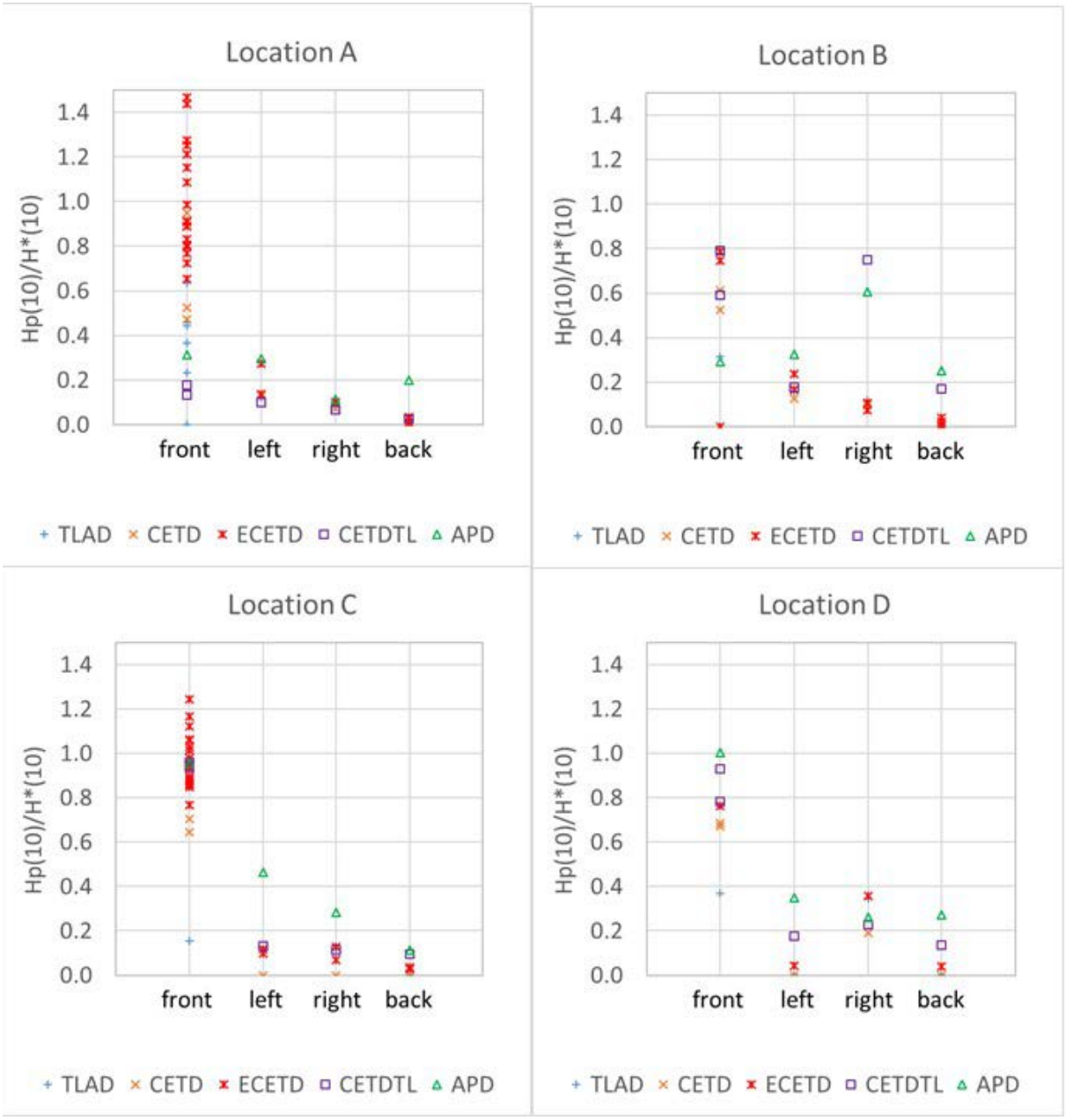

Figure 21. **Results for dosemeters at Positions A, B, C and D.**

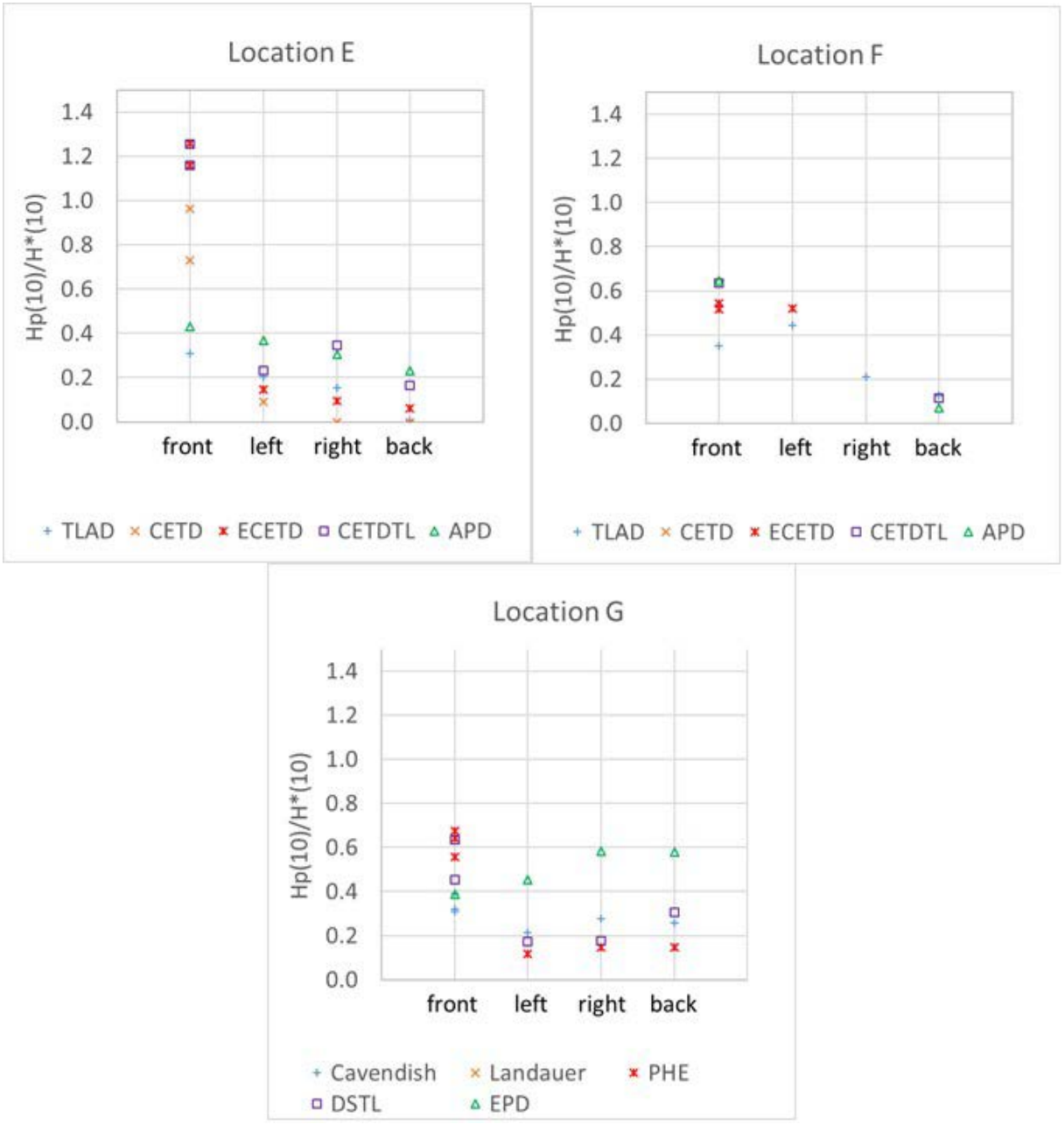

Figure 22. **Results for dosemeters at Positions E, F and G.**

2.8 Personal dose equivalent modelling

When the MCNP model is considered to be fully validated, the $H_p(10)$ will be modelled to generate the reference values to enable calculation of the the personal dosemeter responses. This will be achieved by putting slabs of ICRU tissue in the model at the locations in which the ISO water-filled slab phantoms were exposed. To check the variations across the phantom faces the conversion coefficients will not only be calculated for the centre of the phantom face: smaller tallies will be used to score the field and its variation over the phantom surface.

The established method of Siebert and Schuhmacher [Siebert and Schuhmacher, 1995] will be used and also the direct $Q(L)$ tallying that is now available in MCNP.

2.9 Effective dose estimation

The mapping of the effective dose rate follows the same general procedure as that performed for the PHE Calibration Laboratory and described in detail in Deliverable D9.108. As before, a 'spectral' approach is adopted, in which a family of cones are defined on angled planes to allow the various angle components of the fluence-energy distribution to be determined at each location of interest. These angle components are convolved with appropriate fluence-to-effective dose conversion coefficients, which are binned using a suitably fine energy grid, and then normalized and summed to determine the effective dose rates for individuals located at those positions and orientated in various directions.

To generate the effective dose rate map in the PHE field (D9.108), two cones of half-angle 67.5° were defined with their axes vertical to determine the Semi-Inferior Isotropic (SI-ISO) and Semi-Superior-Isotropic (SS-ISO) components, and 8 tangential cones of 22.5° half-angle were defined with their axes horizontal and at a height of 1.25 m from the floor; the contributions from the 8 horizontal cones were then weighted by a normalization factor (~1.26×) to ensure that the full 4π solid angle was accounted. However, one departure of the SCK•CEN exposure scenario from that at PHE is that its field contains directional components in non-horizontal planes, specifically 'upwards' exposures for individuals standing close to the fuel flask, which was on the floor. So, although the general approach was the same in both cases, this condition necessitated three modifications to the method employed at PHE:

- Fluence contributions in directions with vertical components needed to be calculated. Specifically, this led to eight additional planes and cones at each location being defined, which were directed downwards at an angle of 45°. These cones were distributed rotationally uniformly, relating to individuals facing in the same eight directions as used for the eight horizontal cones. To avoid overlap with each other and the eight horizontal cones, the half-angles of these cones had to be reduced to ~16° (=sin-1[$\pi/8\sqrt{2}$]), with the normalization factor then modified accordingly to account for the fluence 'missed' between the cones.
- Additional fluence-to-effective dose conversion coefficients had to be calculated that corresponded to the eight 'upwards' exposures.
- The opening angle of the 'lower' vertical cone, intended to determine the SI-ISO component of effective dose, also had to be reduced to avoid any double-counting of the fluence tallied by the eight new cones.

The above process will only provide effective doses per neutron emission, which needs to be normalized either to known parameters about the source or to measured benchmark data. Results from the effective dose rate mapping will therefore be obtained when the full validation of the Monte Carlo model is complete, via experimental and computational spectrometry. Once this is achieved, the map will be utilized to facilitate dose calculations from the people tracking.

2.10 People tracking

The indoor positioning system (IPS) was described in detail in D.103 and D.105. During PODIUM, two motion tracking systems were developed to track workers in the two different workplaces considered; interventional radiology and neutron workplaces. In a given realistic neutron workplace, the tracking system should provide the position of the worker into the grid mentioned previously and the direction the person is facing. Thus, the size of the active area of the tracking system will be linked to the area of the measurements grid and hence to the number of cameras to be used. As the tracking system is

making use of infrared depth cameras, the system is limited to indoor environment and low brightness outdoor environment.

In the case of the neutron workplace at SCK•CEN described here, the use of the single camera IPS was sufficient given the size of the grid and being in an indoor facility. The camera was installed outside the grid as shown in Figure 20, where a person can be fully tracked inside the grid.

The calibration software can be used to locate a reference point in the workplace from the camera coordinate system, preferably the origin of the grid, where the coordinates of the tracked body joints will be transformed to (Figure 21). The reference point will be used also to estimate the direction of the person by calculating the angle between the frontal plane that contains the shoulder joints and the plane where the reference point lies on and normal to the floor.

The skeleton tracking was tested during the measurement activities (Figure 22). The recorded sequence simulated realistic actions of a worker moving around the flask and crouching.

The 3D coordinates of the body joints will be provided as an input to the Dose Calculation Application (DCA) in WP3 which will be processed to a position inside the grid and a direction in angles of the worker. The position and the worker can be then used to interpolate within the effective dose map to estimate the dose to the worker per position and direction.

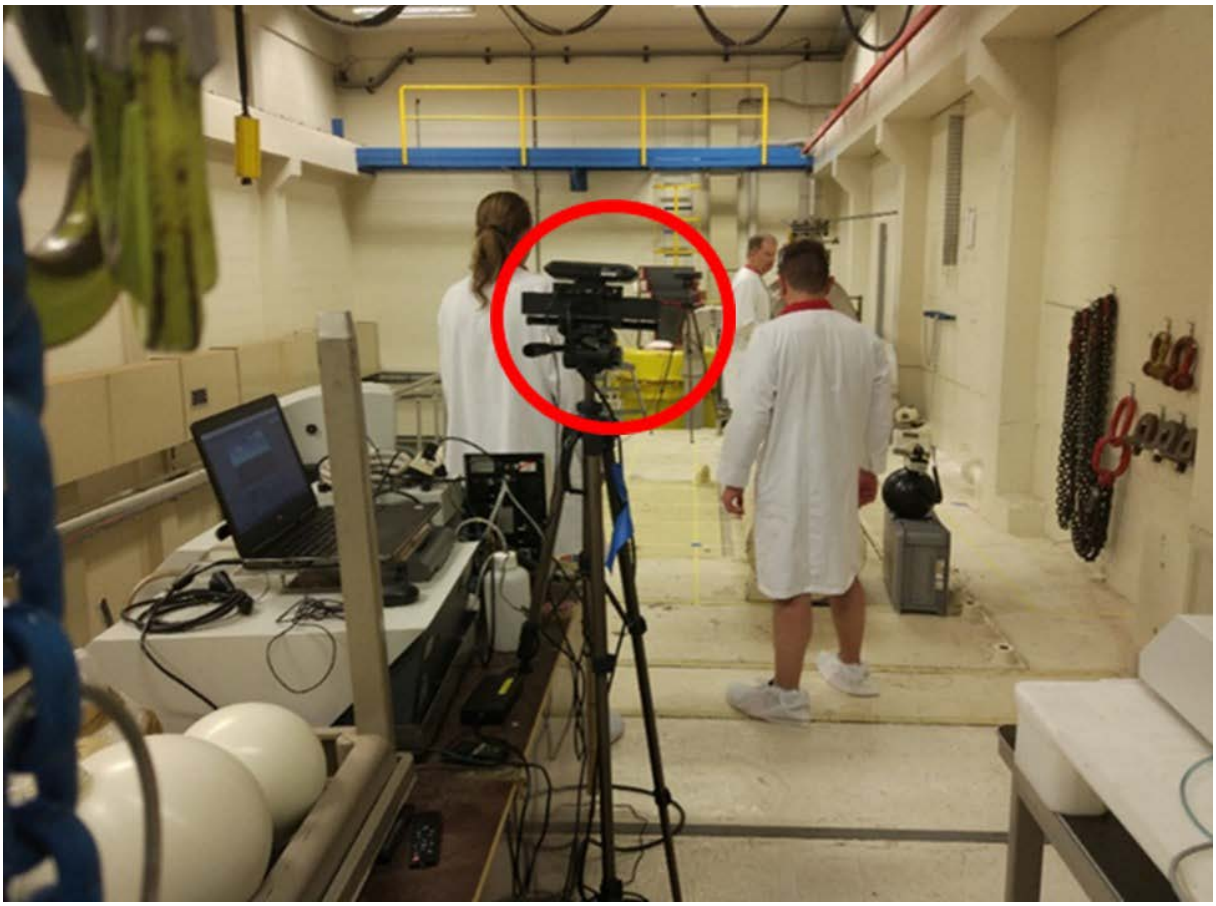

Figure 23. Location of the Kinect shown in the red circle

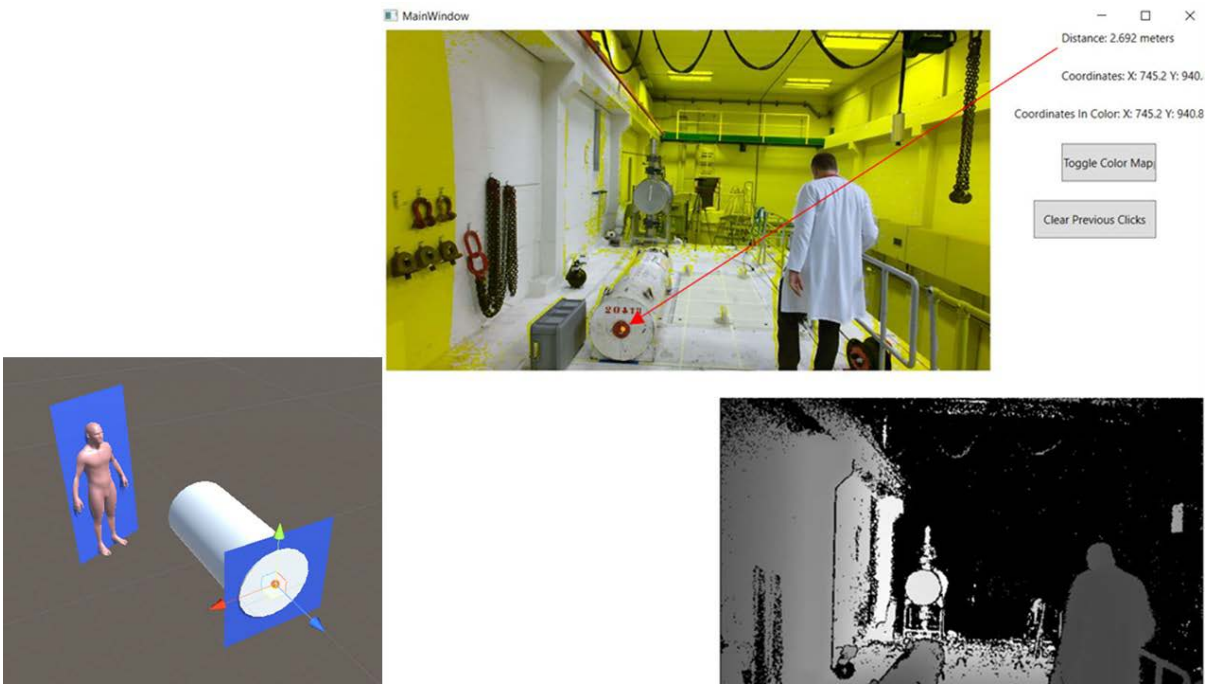

Figure 24. ***The calibration software used to get the coordinates of a reference point***

Figure 25. ***Skeleton tracking recorded sequence during the measurement activities***

3 Summary

These experiments were the first attempt at online dosimetry in a simulated real workplace with significant neutron doses. The field proved to be very good for this pilot project, with significant and measurable neutron dose rates, but relatively low photon dose rates.

One of the biggest concerns for a real workplace was the description of the source for a facility where it was not clearly defined. This issue required the modification of the strategy from that shown in Figure

1 to that in Figure 2. The results are very encouraging, with the field not being very sensitive to the uncertain parameters: the choice of spontaneous fission or (α,n) reactions and the lack of knowledge about the burn-up of the field, do not seem to have created very significant uncertainty. Similarly, the inability to simulate the (α,n) reactions on ^{18}O does not seem to have a significant impact on the results.

The addition of the DIAMON spectrometer, which has the as yet unused potential for direction distribution determination, adds an additional strategy for PODIUM style dosimetry: the method is faster than Bonner spheres and Monte Carlo, so if the results are of acceptable accuracy, dose rate maps could be experimentally determined without the need for lengthy measurements or calculations. This will be expanded upon in the final report as the accuracy of the DIAMON spectra are assessed further.

For this workplace, the results for $H^*(10)$ are providing strong initial validation of the field determinations using spectrometry. For this field the $H^*(10)$ measurements can be good within 10-20%. These could be used for the grid as an approximation for $H_p(10)$ with the PODIUM approach, since this could do better than personal dosemeters which could have an uncertainty of a factor of 4. Given that passive personal dosemeters only yield results after long issue periods, the ability to monitor doses for every shift and even within a shift gives significant benefits in terms of the ALARA approach. This will be aided by the absence of a reporting threshold, which affects personal dosemeters: typically doses below 0.1-0.2 mSv are reported as zero, but in these fields PODIUM could report doses for short occupancy in dose rates of ~ 10 $\mu Sv\ h^{-1}$.

And that is an issue which I am still missing in this deliverable. How do the results compare going from detailed MC simulations, less detailed simulations, detailed spectrometry, basic spectrometry (angular) and just survey instruments. I understand we can not yet include this in this deliverable, but this is actually the goal of this exercise, so this goal should be explained in this conclusion.

The results from this measurement and simulation campaign will be evaluated to assess how reliant the PODIUM approach is on the detail of the Monte Carlo model. Whilst it is always possible to improve Monte Carlo models and make them more realistic, a balance between the effort required and the accuracy needed must be achieved. An improvement on the current state of dosimetry is a clear goal, but then further benefits in terms of ALARA will also result. There are, of course, no standards for acceptable estimation of effective dose, since no system for doing it currently exists. The data available to PODIUM will hence allow the consortium to draw conclusions about the detail required for radiation field determination versus the current state of the art for personal dosimetry. If it is possible to improve on current personal dosimetry using survey instrument measurements and people tracking, then that will be a very attractive workplace option. More field characterization may be required, but the evidence from these experiments is that an effective dose instrument could overcome the need for Bonner sphere evaluations and supporting Monte Carlo models may be viable without complete information about the source and geometry.

The results for personal dose and effective dose can now follow, because the field validation is the necessary initial step. The PODIUM field characterization and people tracking processes for a real workplace are considered to be demonstrated as achievable.

4 References

BEDOGNI, R., DOMINGO, C., ESPOSITO, A. & FERNÁNDEZ, F. 2007. FRUIT: an operational tool for multisphere neutron spectrometry in workplaces. *Nuclear Instruments and Methods in Physics Research Section A: Accelerators, Spectrometers, Detectors and Associated Equipment,* 580**,** 1301-1309.

BURGKHARDT, B., FIEG, G., KLETT, A., PLEWNIA, A. & SIEBERT, B. 1997. The neutron fluence and H*(10) response of the new LB 6411 rem counter. *Radiation Protection Dosimetry,* 70**,** 361-364.

EAKINS, J., HAGER, L., LEAKE, J., MASON, R. & TANNER, R. 2017. Calibration of the GNU and HSREM neutron survey instruments. *Nuclear Instruments and Methods in Physics Research Section A: Accelerators, Spectrometers, Detectors and Associated Equipment,* 852**,** 62-72.

ENSSLIN, N. 1991. The origin of neutron radiation. *Passive Nondestructive Assay of Nuclear Materials***,** 337-356.

GILVIN, P. 2018. Statement of service: PHE Neutron Personal Dosimetry Service.

HAGER, L., TANNER, R., GILVIN, P., EAKINS, J. & BAKER, S. 2017. The impacts of a new electrochemical etch cycle for the Public Health England neutron personal dosimetry service. *Radiation Measurements*.

ISO 2001. Reference neutron radiations - Part 1: Characteristics and methods of production. ISO 8529-1:2001. Geneva: ISO.

KLETT, A. & BURGKHARDT, B. The new remcounter LB6411: measurement of neutron ambient dose equivalent H*(10) according to ICRP60 with high sensitivity. 1996 IEEE Nuclear Science Symposium. Conference Record, 1996. IEEE, 132-134.

LEAKE, J. W., LOWE, T. & MASON, R. S. 2004. Improvements to the Leake Neutron Detector I. *Nuclear Instruments and Methods in Physics Research Section A: Accelerators, Spectrometers, Detectors and Associated Equipment,* 519**,** 636-646.

LUNN, D. J., THOMAS, A., BEST, N. & SPIEGELHALTER, D. 2000. WinBUGS-a Bayesian modelling framework: concepts, structure, and extensibility. *Statistics and computing,* 10**,** 325-337.

MATZKE, M. Unfolding of particle spectra. International Conference Neutrons in Research and Industry, 1997. International Society for Optics and Photonics, 598-607.

OATWAY, W. & MOBBS, S. 2003. Methodology for Estimating the Dose to Members of the Public from the Future Use of Land Previously Contaminated with Radioactivity National Radiological Protection Board. *NRPB-W36 (Chilton: NRPB)*.

OLSHER, R. H., HSU, H. H., BEVERDING, A., KLECK, J. H., CASSON, W. H., VASILIK, D. G. & DEVINE, R. T. 2000. WENDI: an improved neutron rem meter. *Health Phys,* 79**,** 170-181.

OLSHER, R. H. & SEAGRAVES, D. T. 2003. Proton recoil scintillator neutron rem meter. Google Patents.

OLSHER, R. H., SEAGRAVES, D. T., EISELE, S. L., BJORK, C. W., MARTINEZ, W. A., ROMERO, L. L., MALLETT, M. W., DURAN, M. A. & HURLBUT, C. R. 2004. PRESCILA: a new, lightweight neutron rem meter. *Health Phys,* 86**,** 603-612.

PELOWITZ, D. B. 2005. MCNPX user's manual version 2.5. 0. *Los Alamos National Laboratory,* 76.

PELOWITZ, D. B. 2013. MCNP6 user's manual version 1.0. *Vol. LA-CP-13-00634, Rev. 0*.

REGINATTO, M., GOLDHAGEN, P. & NEUMANN, S. 2002. Spectrum unfolding, sensitivity analysis and propagation of uncertainties with the maximum entropy deconvolution code MAXED. *Nuclear Instruments and Methods in Physics Research Section A: Accelerators, Spectrometers, Detectors and Associated Equipment,* 476**,** 242-246.

SASAHARA, A., MATSUMURA, T., NICOLAOU, G. & PAPAIOANNOU, D. 2004. Neutron and Gamma Ray Source Evaluation of LWR High Burn-up UO2and MOX Spent Fuels. *Journal of nuclear science and technology,* 41**,** 448-456.

SHIMANSKAYA, N. 1980a. Energy neutron spectra of the WWER type reactor spent fuel. *Atomnaya Ehnergiya,* 49**,** 315-316.

SHIMANSKAYA, N. 1980b. Neutron radiation yield of spent fuel of VVÉR reactor. *Atomic Energy,* 49**,** 768-770.

SIEBERT, B. & SCHUHMACHER, H. 1995. Quality factors, ambient and personal dose equivalent for neutrons, based on the new ICRU stopping power data for protons and alpha particles. *Radiation Protection Dosimetry,* 58**,** 177-183.

SOPPERA, N., DUPONT, E., BOSSANT, M. & BANK, O. N. D. 2017. JANIS Book.

TANNER, R. J., MOLINOS, C., ROBERTS, N. J., BARTLETT, D. T., HAGER, L. G., JONES, L. N., TAYLOR, G. C. & THOMAS, D. J. 2007. Practical implications of neutron survey instrument performance. Didcot: Health Protection Agency.